

HiSST: 4th International Conference on High-Speed Vehicle Science Technology

22-26 September 2025, Tours, France



Laminar-to-Turbulent Transition on the BOLT geometry at Mach 7

Loïc Sombaert ¹, Mathieu Lugrin ², Guillaume Bégou ³, Sébastien Esquieu ⁴, and Reynald Bur ⁵

Abstract

This support paper for the oral presentation at the HiSST conference investigates the laminar-to-turbulent transition over the BOLT geometry, based on experimental data acquired in the ONERA R2Ch hypersonic blowdown wind tunnel using a 1/3-subscale model at Mach 7. Infrared thermography and high-speed wall-pressure measurements (PCB sensors) were obtained across a broad range of freestream Reynolds numbers, from fully laminar to well-developed turbulent regimes. Transition typically appears firstly in the outboard region of the geometry, characterized by the appearance of two symmetric heating lobes away from the centerline. Particular attention is given to this region, where a high-frequency instability near 150 kHz is consistently detected in the Power Spectral Densities at Reynolds numbers around 5×10^6 m⁻¹. A lower-frequency bump near 20 kHz is also observed, though less distinctly. To investigate the physical origin and nature of these instabilities, a Linear Stability Theory (LST) analysis is conducted based on numerically computed laminar baseflows. Results from this analysis suggest that the observed spectral bumps are associated with the amplification of the second Mack mode and traveling crossflow instabilities. This is consistent with existing literature, as these two instability mechanisms are commonly identified as dominant in hypersonic boundary-layer transition over complex three-dimensional geometries. However, the application of classical LST to such a complex three-dimensional geometry leads to relatively low N-factors, below 1.5, despite the experimental data clearly indicating the occurrence of transition. This discrepancy highlights the limitations of LST in predicting transition onset in realistic configurations, where non-parallel effects and mode interactions may play a significant role and are not captured by local, linear analyses.

Keywords: Hypersonic Flow, Boundary-layer Transition, Linear Stability Analysis, Complex geometry.

1. Introduction

Laminar-to-turbulent boundary-layer transition remains a major source of uncertainty in predicting heating and aerodynamic loads at hypersonic speeds [1, 2]. Turbulent breakdown results in intense wall heating (up to 8 times higher than the laminar state) along with a significant increase in viscous drag [3]. Accurate consideration of the transition process is thereby key to the design of next-generation hypersonic vehicles, as it directly impacts thermal protection systems selection and sizing, trajectory prediction, stability and maneuverability, propulsive efficiency, radar signature, and onboard sensor operation [4]. Thus, the hypersonic transition community is shifting toward physics-based prediction models [5], going beyond semi-empirical methods restricted to a small range of flight conditions and geometries. Yet, such effort requires a deeper understanding of the mechanisms driving transition in complex configurations.

It is known for decades that the transition process is affected by a wide variety of factors (Mach number, Reynolds number, freestream perturbations, angle of attack, surface roughness, pressure gradient, nose bluntness...) [6]. In wall-bounded flows, freestream disturbances can trigger unstable waves in the boundary-layer, which acts as a selective filter. These instabilities amplify linearly first, non-linearly then, to finally lead to turbulence. Wind tunnel testing suffers from a different freestream environment from flight conditions (with noise levels 10 to 100 times higher in conventional facilities), resulting in earlier

¹Ph.D. Student, DAAA ONERA, Institut Polytechnique de Paris, 92190, Meudon, France.

² Research Scientist, DAAA ONERA, Institut Polytechnique de Paris, 92190, Meudon, France.

³ Research Scientist, DAAA ONERA, Institut Polytechnique de Paris, 92190, Meudon, France.

⁴Research Engineer, CEA-CESTA, 15 Avenue des Sablières, 33114, Le Barp, France.

⁵ Research Director, DAAA ONERA, Institut Polytechnique de Paris, 92190, Meudon, France.

transition onset. Combining experimental data with numerical approaches becomes thereby a necessity for a better understanding of the transition process and, ultimately, extrapolating the data to flight conditions. The USAF/AFOSR (U.S. Air Force Office of Scientific Research) HIFIRE program exemplifies the value of this multi-faceted approach. Initiated in 2008 [7], it featured two flights (1 and 5b) which delivered high-quality data supporting the development and validation of mechanism-based transition models, particularly for second Mack mode and crossflow instabilities [8].

2. The BOLT geometry

Building on the success of the HiFIRE flights, the AFOSR introduced the BOundary Layer Transition (BOLT) flight experiment in 2017 [9]. The scientific objective is to investigate the transition mechanisms on a complex geometry that would challenge existing transition prediction tools at high Mach numbers (from five to seven). In this way, BOLT features a low-curvature concave surface with highly-swept leading edges [10]. Over the years, a broad international community -including academia, industry, and governmental research organizations- has joined forces to advance the comprehension of transition mechanisms over this geometry.

Three flight experiments have been launched since the beginning of the project: BOLT-1a (2021) [11, 12], BOLT-2 (2022) [13], and BOLT-1b (2024) [14]. These flight experiments have been complemented by extensive pre- and post-flight computational and experimental investigations. Early simulations have revealed the complexity of the flowfield induced by the geometry, characterized by a pair of counterrotating vortices near the center plane, generated by the 3D nose, as well as multiple co-rotating vortices in the outboard regions that modulate the heat-flux at the wall [15]. These flow structures are typical of those observed in three-dimensional geometries and, by extension, in realistic forebody configurations. In conventional facilities, transition over this geometry typically appears as symmetrical lobes with respect to the centerline [16]. Various investigations (stability analyses (LST, PSE), DNS, and experiments) at Mach 6 have provided insights into the dominant instability mechanisms on BOLT. Crossflow instabilities (both stationary and traveling) are believed to be the primary drivers of transition. However, experimental data at Mach 7 from DLR [17], as well as from our previous work in R2Ch [18], revealed a high-frequency instability (150-200 kHz) that was absent at Mach 6, raising questions about its role in transition. Subsequent linear stability analyses on the DLR conditions conducted by NASA Langley Research Center and the Johns Hopkins University - Applied Physics Laboratory suggest that this instability is associated with the second Mack mode [19].

This paper aims to enhance the interpretation of experimental data acquired in the R2Ch facility by using the linear stability analysis framework recently developed at ONERA/DAAA.

3. Experimental Setup

For the sake of conciseness, only the key elements of the experimental setup are presented here. The reader is referred to [18] for a detailed description of the facility, instrumentation, and data processing.

3.1. The R2Ch Facility

The experimental campaign was conducted in the cold hypersonic blow-down facility R2Ch[†] at ONERA (Meudon Centre) [20]. It is a conventional wind tunnel that maintains hypersonic conditions for 10 to more than 60 s of testing. A Mach 7 nozzle is used in this study. Reservoir pressure (p_0) can range from 0.5 up to 80 bars. Dry air is heated up to prevent liquefaction up to a reservoir temperature (T_0) of 750K. Freestream quantities (p_∞ , T_∞ , p_∞ , and p_∞) are then derived assuming an isentropic expansion through the nozzle, considering a thermally and calorically perfect gas. The freestream dynamic viscosity (p_∞) is computed using Sutherland's law of viscosity. The freestream noise level of the facility has been measured to $p'/p_\infty=1.51\%$ at $p_\infty=5$, within the standards of conventional tunnels, although this value is not sufficient to characterize the noise environment of the facility [21]. Work is under progress regarding a proper freestream characterization of R2Ch [22].

HiSST-2025-256 L. Sombaert, M. Lugrin, G. Bégou, S. Esquieu, and R. Bur

[†]Facility overview video: https://www.youtube.com/watch?v=YqIrpAQsa6Y

3.2. Subscale model description

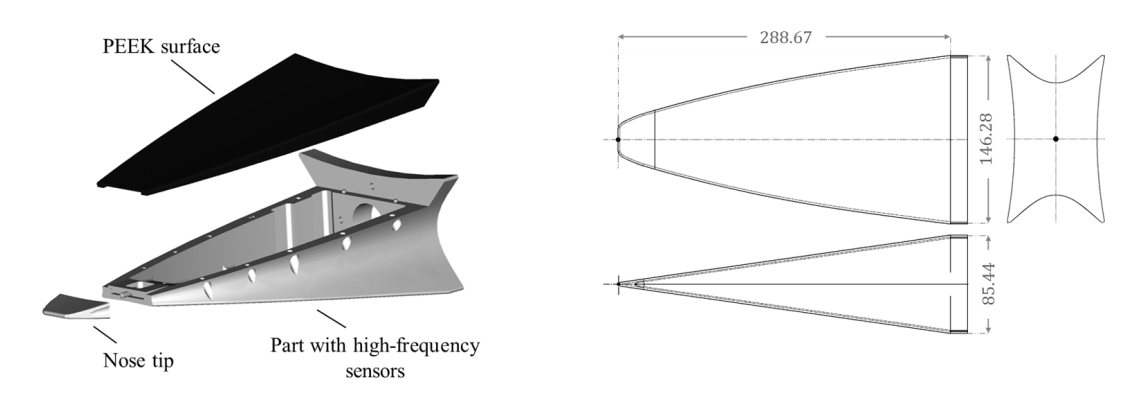


Fig 1. 1/3-subscale model dimensions (mm) and exploded view.

The model is a 1/3-subscale model of the BOLT-1 flight geometry. It has an overall length of 288.67 mm. It is composed of three parts: a main structure on which the nose and the second surface of experiment are inserted (Fig. 1). This second surface of experiment is made up of PEEK, a low thermal conductivity, high emissivity, thermo-plastic material that can resist the harsh environment of the facility and, therefore perfectly suited for infrared thermography measurement under hypersonic conditions. The campaign is conducted at 0° angle of attack and 0° yaw.

3.3. Instrumentation, Acquisition, and Processing

3.3.1. Infrared (IR) Thermography

The temperature distribution on the PEEK surface is recorded with a FLIR SC7600 infrared camera (IR range: $3-5.1\,\mu\text{m}$, resolution: $640\times512\,\text{px}$, frame rate: $100\,\text{Hz}$). Details on the IR setup associated with this campaign can be found in [18], and details on the ONERA in-house reduction model in [23, 24] (calibration, model tracking and mapping...). Heat-flux (Q_w) is then computed using the FLUX1D model, based on the following assumptions: the resolution of the one-dimensional heat equation with lateral conduction effect correction, the model can be treated as a semi-infinite slab, and uniform and temperature dependent thermal properties of the material. Wall heat-transfer is presented in this paper using the Stanton number (St) definition:

$$St = \frac{Q_W}{\rho_\infty u_\infty c_p (T_r - T_W)}$$

where the recovery temperature is computed by $T_r = T_{\infty}(1 + r\frac{\gamma - 1}{2}M_{\infty}^2)$ with values of $c_p = 1004$ J/kg.K and r = 0.89 (turbulent recovery factor).

3.3.2. High-Speed Wall Pressure Measurements (PCB132-B38)

The PCB 132 series sensors allow to measure frequency content from 11 kHz up to 1 MHz. In this study, among the 11 sensors installed on the model, only the 4 sensors located in the outboard region are considered. They are listed in Table 1 and their locations on the model are highlighted in Fig. 2. They are linked to a 4-channel PCB 482-C05 signal conditioner. Neither additional hardware amplification nor filtering is made. The output signal is sampled at 3.3 MHz by a NI-PXIe6376 (16-bit). Power Spectral Densities (PSD) are computed from the 2s acquisition (6.6 million data points) using Welch's method with a Hanning window (2000 blocks of 6666 samples with a 50% overlap, $\Delta f = 500\,\text{Hz}$). A pre-run measurement is always performed before a test so that the electrical noise floor level is known for all the conditions investigated.

Sensor	x, mm	z, mm
PCB04	174.07	31.75
PCB06	212.17	31.75
PCB08	237.57	31.75
PCB11	278.84	31.75

Table 1. PCB sensor locations.

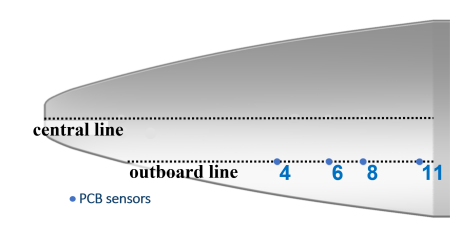


Fig 2. PCB132 locations on the model.

4. Numerical Setup

4.1. Condition of Interest

The simulation presented in this paper is based on an experimental condition performed during the R2Ch campaign. The flow conditions were selected to be representative of the experiments in which valuable data in the transitional regime were acquired. This corresponds to a relatively low Reynolds number for the facility ($Re_{\infty}=5.24\times10^6~\text{m}^{-1}$). In conventional tunnels, this Re_{∞} is associated with the onset of transition in the outboard region of the BOLT geometry [25]. Corresponding freestream conditions are summarized in Table 2. The wall temperature T_{w} is determined using the averaged IR thermography data prior to the start of the test.

M_{∞}	<i>Re</i> _∞ [m ⁻¹]	<i>u</i> _∞ [m.s ⁻¹]	p∞ [Pa]	<i>T</i> _∞ [K]	<i>T</i> _w [K]
7.0	5.24×10^{6}	967.0	223.1	47.5	311

Table 2. Freestream conditions of the study based on the R2Ch experimental campaign.

4.2. Structured Mesh Generation

A 1/3-scale BOLT model is used in the simulations to replicate the configuration from the experiments (for dimensions, see Fig. 1). Exploiting the geometrical symmetries of the configuration, only one quarter of the full geometry is considered to reduce the computational cost (Fig. 3 (*left*)). The design of the structured mesh has been carried-out using the ICEM-CFD software developed by ANSYS. Proper shock resolution is achieved through an iterative shock-fitting procedure based on numerous laminar flow simulations. The sharpness and position of the shock was examined across the various grids, until the numerical dissipation remained sufficiently low. In addition, a dedicated block has been introduced in the vicinity of the surface to accurately resolve the boundary-layer and ensure adequate resolution of the near-wall gradients. On this geometry, one of the main challenge lies in accurately meshing the nose region, particularly in the area where the two-dimensional blunt nose and the leading edge merge (Fig. 3 (*center*)). This requires special treatment to prevent singularities and ensure a proper mesh quality. An

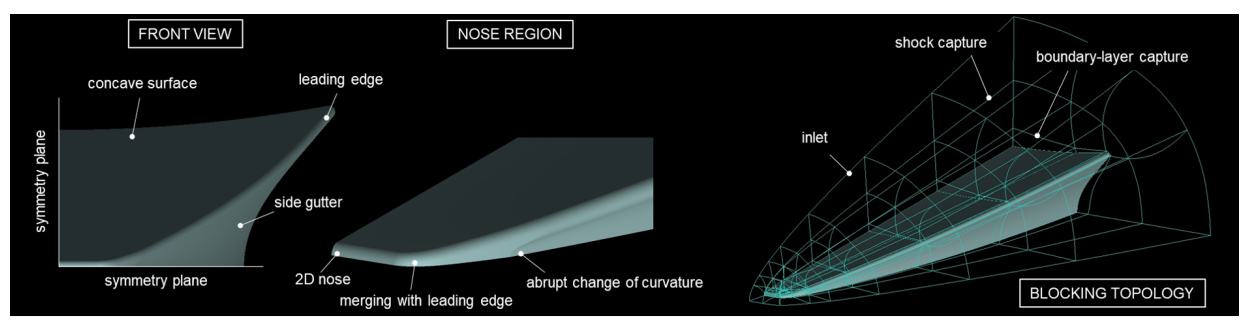


Fig 3. Front view of the quarter BOLT geometry (*left*), detailed view of the nose region highlighting geometric complexities (*center*), and blocking topology (93 blocks) used for the structured mesh generation with icem-cfd (*right*).

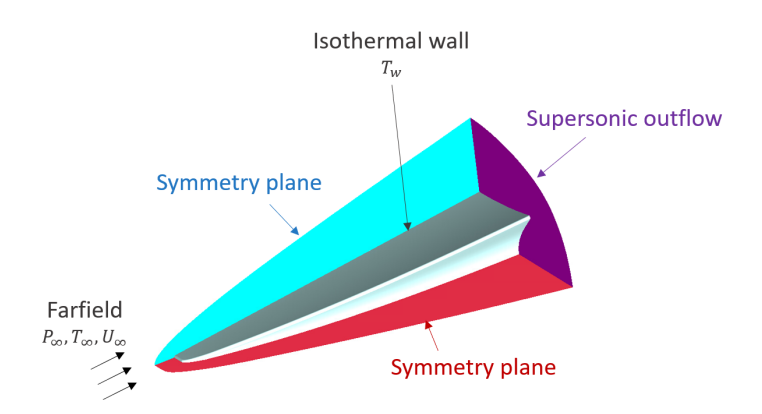


Fig 4. Boundary conditions considered in the study.

O-grid block structure has therefore been selected in this region. The resulting topology contains a total of 93 blocks to entirely mesh the domain.

4.3. Baseflow Computation

4.3.1. Setup

The governing equations used here to compute the laminar baseflow are the compressible Navier-Stokes equations. Simulations have been performed with the ONERA elsA solver. Boundary conditions are displayed in Fig. 4. The inlet boundary condition corresponds to the shock surface extracted from preliminary simulations which has been magnified by a certain factor. Two symmetry planes are imposed: one at the midspan of the main upper surface, and the other at the centerline of the gutter surface. At the outlet, a supersonic outflow condition is applied. A steady solution is obtained via local time stepping using an implicit Backward Euler scheme. The convective fluxes are computed using a second-order reconstruction and an AUSM+ scheme [26]. Viscous fluxes are computed using a second order centered scheme on five points.

4.3.2. Convergence Study

In addition to ensuring residual convergence for each simulation, particular attention was paid to verifying the spatial convergence of the computed flow. This was achieved by conducting a grid refinement study using several meshes of increasing resolution. A summary of the mesh characteristics and spatial distributions is presented in Tables 3 and 4. All grids share the same blocking topology. They were designed to ensure sufficient near-wall resolution to accurately capture the wall heat-flux.

The objective here is to confirm that key flow features (such as vortical structures, shock locations, boundary-layer profiles, and surface heat flux distributions) were no longer sensitive to grid resolution. Figure 5 illustrates the impact of grid quality and resolution on the prediction of the centerline vortical structures at $x=0.288\,\mathrm{m}$, near the end of the computational domain. The figure shows the sensitivity of the counter-rotating vortex to mesh refinement. The simulation using the 30-million-cell grid exhibits significant limitations in capturing the spanwise velocity gradients associated with the vortical structure. In contrast, the 230-million and 410-million-cell grids yield nearly identical results, indicating that spatial convergence of the flowfield has been achieved in this region.

	streamwise	wall-normal	spanwise*	leading-edge	boundary-layer
Grid 1 (74 × 10 ⁶)	990	225	205	70	90
Grid 2 (231 \times 10 ⁶)	1400	335	315	100	110
Grid 3 (413 \times 10 ⁶)	1770	370	410	120	125

Table 3. Mesh distributions considered for the convergence study. (*The spanwise node count refers only to the main surface of the geometry.)

HiSST-2025-256

Page | 5

Laminar-to-Turbulent Transition on the BOLT geometry at Mach 7

Copyright © 2025 by the authors

	streamwise [µm]	wall-normal [μ m]	spanwise [µm]
Grid 1	1270	32	373
Grid 2	882	32	242
Grid 3	420	32	193

Table 4. Mesh dimensions at the wall along the symmetry plane at the downstream end of the numerical domain (x = 288.67 mm, z = 0 mm).

4.4. Linear Stability Analysis

4.4.1. Equations

Considering the Navier–Stokes equations written in a compact form as:

$$\mathcal{N}(\mathbf{q}) = \frac{\partial \mathbf{q}}{\partial t}$$

where $\mathcal N$ denotes the Navier–Stokes operator, and $\mathbf q=(\rho,\rho\mathbf u,\rho E)$ is the conservative state vector. Each flow variable is assumed to be decomposable into a base component $\overline{\mathbf q}$ and a fluctuating perturbation $\mathbf q'$, such that $\mathbf q=\overline{\mathbf q}+\mathbf q'$. Since the focus of this work is on the laminar-to-turbulent transition process, the base component $\overline{\mathbf q}$ refers here to a steady laminar baseflow, which serves as the reference state for the linear stability analysis. The LST analysis focuses on the spatial or temporal evolution of the perturbation field $\mathbf q'$. In order to remain within the linear regime, these perturbations are assumed to be of small amplitude relative to the baseflow ($\mathbf q'/\overline{\mathbf q}\ll 1$). This assumption only holds in the first stages of the transition process. Moreover, as LST is inherently a local stability approach in which one-dimensional baseflow profiles are analyzed independently at each streamwise location, it relies on the parallel-flow assumption (the streamwise variation of the baseflow is neglected).

The perturbations are assumed to take the form of harmonic waves, expressed as:

$$\mathbf{q}' = \hat{\mathbf{q}}(y) e^{i(\alpha x + \beta z - \omega t)}$$

where α and β are the streamwise and spanwise wavenumbers, respectively, and ω is the angular frequency of the disturbance. In this study, a spatial stability analysis is employed, in which the frequency ω is taken as real and the streamwise wavenumber $\alpha = \alpha_r + i\alpha_i$ is complex. As a result, the perturbation takes the form:

$$\mathbf{q}' = \hat{\mathbf{q}}(y) e^{-\alpha_i x} e^{i(\alpha_r x - \omega t)}$$

where α_i represents the spatial growth rate of the instability. The stability of the flow depends on the sign of the growth rate. A negative value of α_i indicates an exponentially growing wave as it propagates

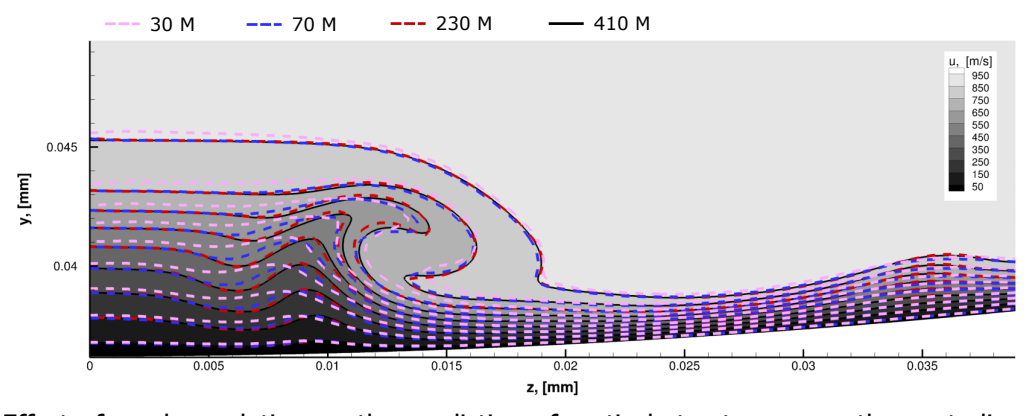


Fig 5. Effect of mesh resolution on the prediction of vortical structures near the centerline at x = 0.288 m. Results are shown for grids ranging from 30 million to 410 million cells, highlighting the improved resolution of flow structure with increasing mesh density.

downstream, thereby an unstable flow.

This LST analysis is carried out with the ONERA in-house code MARCEL. This code allows solving the local linear dimensionless compressible stability equations for boundary-layer profiles by solving a generalized eigenvalue problem. Therefore, for a given baseflow $\overline{\mathbf{u}}(v)$ and $\overline{T}(v)$ at a specific streamwise location, and for a prescribed pair of spanwise wavenumber β and frequency ω , the linear stability problem seeks eigenpairs ($\hat{\mathbf{q}}$, α) that satisfy the stability equations.

An important quantity derived from LST is the so-called N-factor, which provides a measure of the cumulative amplification of a given instability mode along the streamwise direction. It is formally defined

$$N(x) = \int_{x_0}^{x} -\alpha_i(\xi) \,\mathrm{d}\xi,$$

where ξ denotes the streamwise coordinate used as the integration variable. The integration is performed from a reference location x_0 , typically where the mode first becomes unstable ($\alpha_i < 0$), up to the location x. This formulation assumes that the instability amplitude evolves as $A(x) = A_0 e^{N(x)}$, where A_0 is the initial amplitude of the perturbation. The N-factor thus quantifies the logarithmic growth of a disturbance mode $(N = \log(A/A_0))$ and is central to the interpretation of transition scenarios in boundary-layer flows.

One important limitation of the LST approach is that it does not provide any information regarding the absolute amplitude of the perturbations. In other words, the method identifies whether a given disturbance mode is amplified or attenuated, but it does not predict how large the perturbation actually is in the boundary-layer at a given location. As a result, LST cannot, on its own, determine whether the transition to turbulence will actually occur. To address this, a typical approach to determine whether or not transition should occur is the e^N method, where transition is assumed to occur once N exceeds a critical value, often derived from experimental correlation [27].

4.4.2. Practical Example of MARCEL Stability Code

In order to illustrate the local linear stability analysis performed in this study, a representative example is presented based on a boundary-layer profile extracted on the main surface of BOLT (Fig 6). The selected profile corresponds to a streamwise location near the aft region of the body. The extraction of boundary-layer quantities is made following the method presented in [28].

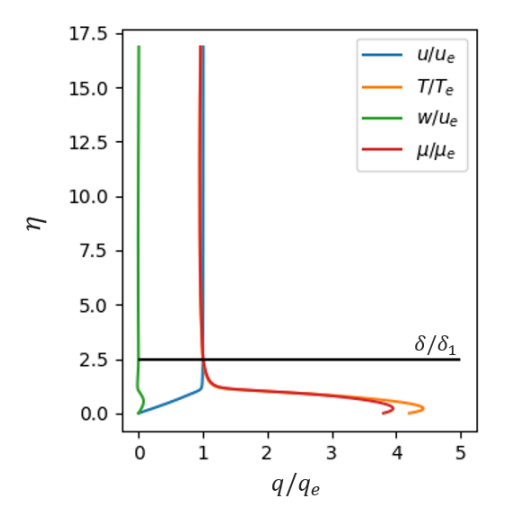


Fig 6. Non-dimensional boundary-layer profiles in the MARCEL framework (on the BOLT geometry: $x = 278.84 \,\mathrm{mm}$ and $z = 31.75 \,\mathrm{mm}$).

Below is an example for a planar mode ($\beta = 0 \text{ m}^{-1}$). One of the main challenges in conducting a LST analysis lies in providing an accurate initial guess for the instability parameters, particularly the

HiSST-2025-256 Page | 7 frequency and the complex streamwise wavenumber ($\alpha = \alpha_r + i\alpha_i$). These values serve as input for the eigenvalue solver and must be sufficiently close to the true eigenmode to ensure convergence towards a physically relevant solution. When a sufficiently close guess is made, it lead in this example to the convergence towards a high-frequency instability mode ($\alpha_i < 0$) exhibiting characteristics consistent with the second mode (Fig. 7), a strong signature of pressure within the boundary-layer with a peak close to the wall [29] (Fig. 7, highlighted by the red box). Once an unstable mode is identified at a given

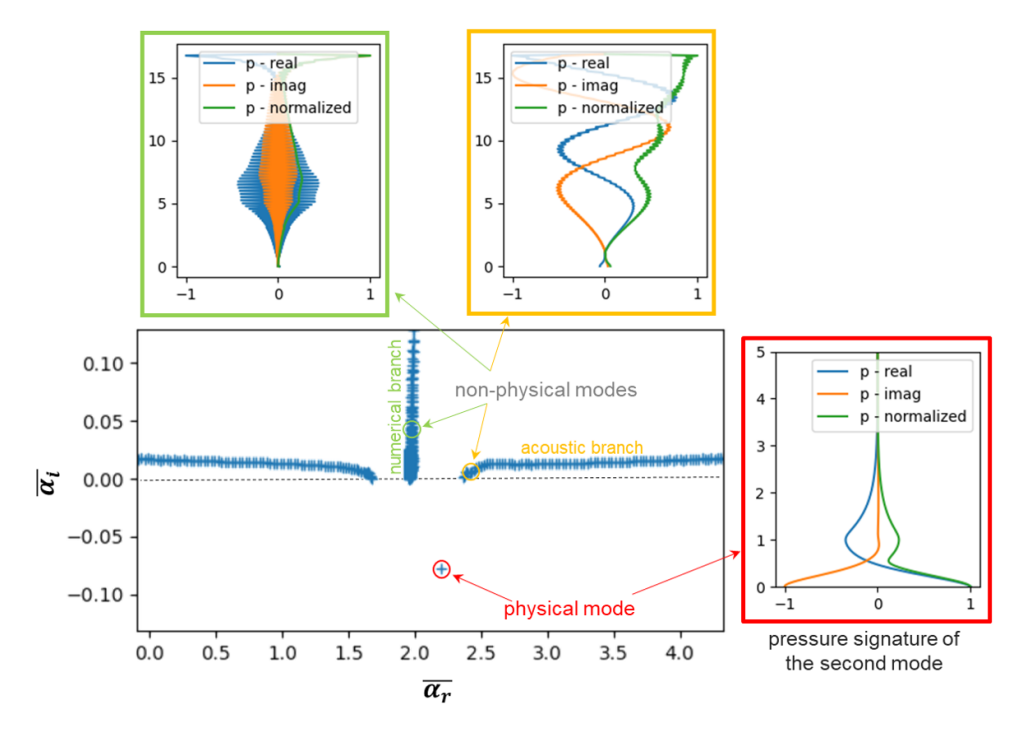


Fig 7. Example of a spectrum showing a physical mode ($f = 160 \, \text{kHz}$, $\beta = 0$)

location, it can be spatially tracked along the flow direction. In this work, the most effective strategy was found to be a downstream-to-upstream tracking approach: starting from a point where the mode is strongly amplified, the mode is then tracked upstream along the flow. While the common practice is to follow the streamlines of the baseflow for such tracking, we chose here, for simplicity, to follow the mesh lines. Although this may introduce deviations when the mesh is not aligned with the streamlines (particularly at the front of the BOLT geometry), this approximation remains reasonable in the aft region, where the alignment streamlines/grid is more favorable.

5. Experimental Results

A comprehensive analysis of the experimental results acquired during the campaign is provided in [18]. The present discussion focuses instead on a qualitative interpretation of selected data, aimed at guiding the stability analysis and identifying the main transition features observed in the measurements.

5.1. Infrared Thermography

Figure 8 presents the non-dimensional heat-transfer distributions, expressed as $St\sqrt{Re_L}$, obtained for three different freestream Reynolds number conditions at Mach 7. The results highlight the excellent flow symmetry with respect to the centerline. It also shows the influence of the freestream Reynolds number on the wall heat-flux. As expected, low- Re_∞ case exhibit lower heat-transfer levels, whereas high- Re_∞ conditions lead to the development of significantly higher heating rates. Although this relationship does not always strictly hold (particularly for complex 3D configurations), regions of lower heat transfer are generally indicative of laminar flow, while areas exhibiting higher heat transfer typically correspond to turbulent regimes. Moreover, an increase in wall heating along the streamwise direction is often associated with transition. Based on this simplified interpretation of wall heat transfer levels, a preliminary analysis of the data reveals a clear influence of the freestream Reynolds number. At low

values ($Re_{\infty} = 1.74 \times 10^6 \,\mathrm{m}^{-1}$), the heat-flux distribution is consistent with a fully laminar boundarylayer: overall heating levels remain low. Difference appears between the centerline and the outboard regions, with the centerline exhibiting lower heat-flux due to a thicker boundary-layer. As the freestream Reynolds number increases ($Re_{\infty} = 6.11 \times 10^6 \, \text{m}^{-1}$), localized increases in heat transfer are observed in the outboard regions of the model, forming two distinct lobes symmetrically distributed with respect to the centerline. This pattern is indicative of the onset of transition. Finally, at the highest Reynolds numbers investigated ($Re_{\infty} = 29.9 \times 10^6 \, \text{m}^{-1}$), the previously identified heating lobes are observed to shift significantly upstream. An increase in heat transfer along the centerline also appears. Furthermore, the reduction in heat-flux levels downstream, may be interpreted as a fully turbulent flow.

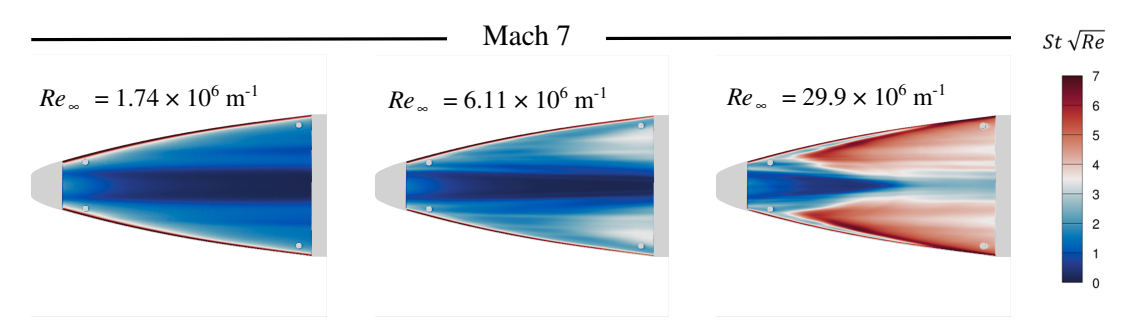


Fig 8. Stanton number distribution for three Reynolds number conditions at $M_{\infty} = 7$.

5.2. High-Speed Wall Pressure Fluctuation Measurements in the Outboard Region

In addition to wall heat-flux distributions, which provide a global view of the transition process, the analysis of instantaneous wall pressure fluctuations offers valuable insight into the local state of the boundary-layer. Figure 9 presents pressure signals acquired by a sensor located in the outboard region (PCB11), for three distinct freestream Reynolds numbers representative of laminar ($Re_{\infty} = 3.24 \times 10^{-2}$ $10^6 \,\mathrm{m}^{-1}$), transitional ($Re_{\infty} = 5.24 \times 10^6 \,\mathrm{m}^{-1}$), and turbulent ($Re_{\infty} = 8.12 \times 10^6 \,\mathrm{m}^{-1}$) regimes, as independently identified from infrared thermography. The transitional regime reveals the presence of localized wavepackets, indicative of convectively amplified instabilities developing within the boundarylayer. To further investigate their nature, power spectral densities (PSDs) were computed and compared across a large range of Reynolds numbers. Two frequency bands of interest emerge.

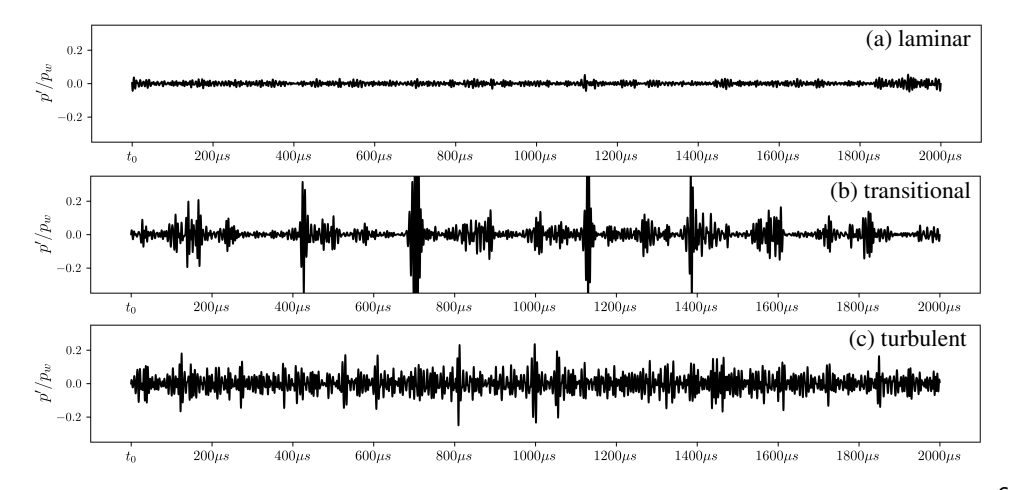


Fig 9. Instantaneous wall pressure fluctuations signal from PCB11. (a) $Re_{\infty} = 3.24 \times 10^6 \, \text{m}^{-1}$, (b) $Re_{\infty} = 5.24 \times 10^6 \,\mathrm{m}^{-1}$, and (c) $Re_{\infty} = 8.12 \times 10^6 \,\mathrm{m}^{-1}$. For clearer representation, the signal has been filtered between 100 and 250 kHz.

First, a bump consistently appears between 100 and 200 kHz for cases spanning $Re_{\infty}=2.79$ to 5.06×10^6 m⁻¹. The peak frequency of this bump slightly increases with Reynolds number (i.e., thinning of the boundary-layer) and shift towards higher frequencies. As the flow gets closer to the turbulent regime, this bump flattens, consistent with the broadband nature of turbulence. The presence of such

HiSST-2025-256 Page | 9 Copyright © 2025 by the authors high-frequency instability strongly suggest its association with the second Mack mode instability, a well-known mechanism in hypersonic boundary-layers. A second, less pronounced bump is observed in a lower frequency range (from approximately 11 to 50 kHz for $Re_{\infty}=2.79$ to $6.11\times10^6\,\mathrm{m}^{-1}$). The frequency range could match traveling crossflow instabilities, which are frequently encountered in three-dimensional boundary-layers.

The linear stability analysis presented in the following section aims to investigate these two frequency ranges to identify whether or not these bumps are related to unstable modes.

6. Laminar Baseflow Analysis

Figure 11 presents the computed laminar baseflow obtained for the flow conditions listed in Table 2 on the 231-million grid (used for the LST analysis). The characteristics of the BOLT flowfield are well captured, with the formation of a pair of counter-rotating vortices developing along the main surface and surrounding the centerline region, as observed in previous numerical investigations. The boundary-layer thickness exhibits significant spanwise variation. Along the centerline, it grows substantially, reaching approximately 20 mm at the end of the computational domain, as a result of the vortex-induced upwash. In contrast, the outboard regions maintain significantly thinner boundary-layers, typically on the order of a millimeter. At this Reynolds number, the development of a vortex in the outboard region further modulates the local boundary-layer thickness spanwise. This modulation leads to surface heat-flux variations, with upwash zones corresponding to reduced heating and downwash zones to increased heating. Our PCB sensors are located in the vicinity of this vortex.

A direct comparison between the laminar simulation and experimental measurements is presented in Figure 12 (left), which shows the relative deviation in Stanton number ($(St_{exp} - St_{lam})/St_{lam} \times 100$). This provides valuable insights into regions of transition, although it does not allow for a precise determination of the transition onset without defining a somewhat arbitrary threshold. Along the centerline, a very good agreement is observed between the laminar computation and experimental data, confirming the presence of a laminar regime in this region. In contrast, in the outboard regions, a significant discrepancy develops downstream, consistent with the presence of transition.

Figure 12 (*right*) shows the corresponding experimental heat-flux distribution, with the 25% relative difference contour superimposed in black. This threshold was chosen as it was shown to correlate well with experimentally determined transition onsets [18]. This transition front exhibits a distinct sawtooth pattern, which closely follows the heating streaks emerging from the leading edges. These streaks, ab-

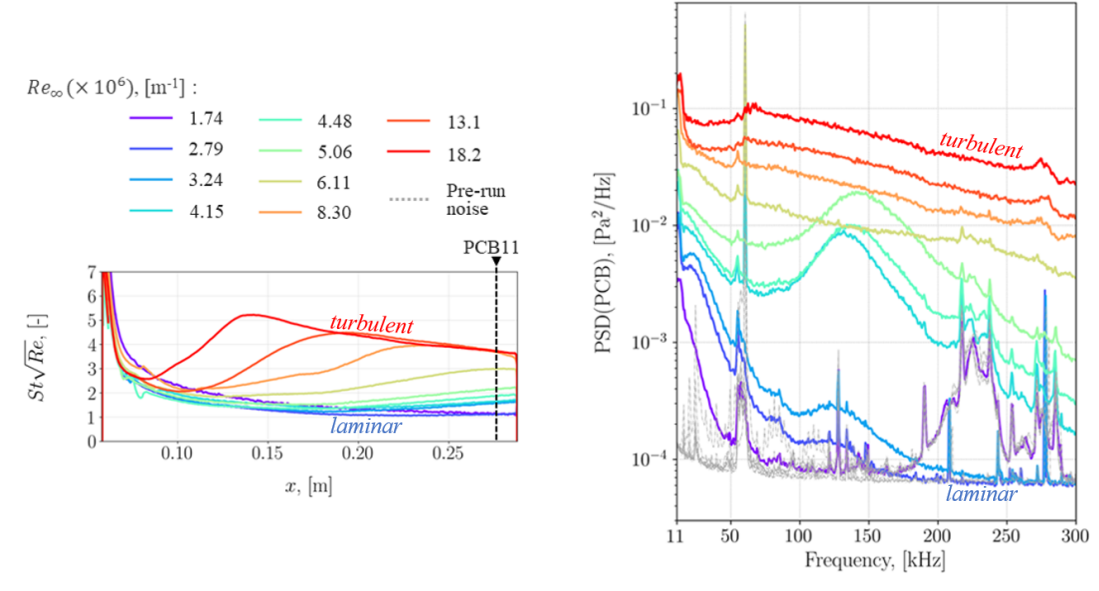


Fig 10. Power Spectral Densities from PCB11 for various freestream conditions (*right*). Wall heat-flux data associated with the run (*left*) and PCB11 location.

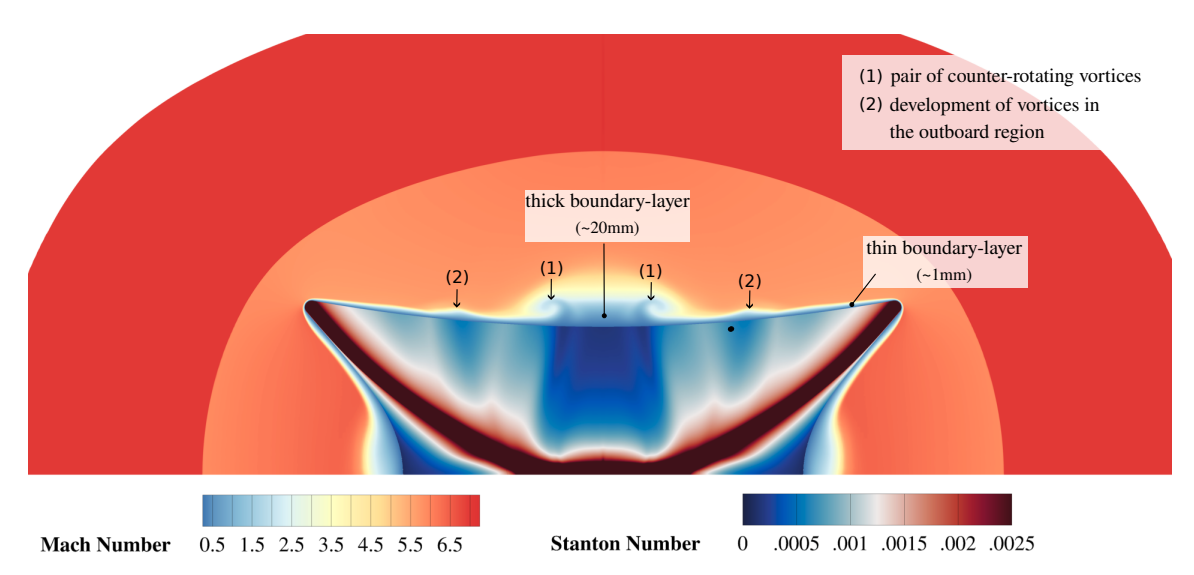


Fig 11. Laminar baseflow used for the LST analysis. Mach number contour at the x=288 mm plane (*background*) and surface of BOLT colored by Stanton number. The domain is mirrored around the symmetry plane (z=0 mm). PCB11 location is superimposed on the surface with a black dot.

sent from the laminar simulation, are indicative of the presence of vortical structures.

Such a pattern could plausibly be attributed to stationary crossflow vortices, which are known to be highly sensitive to surface roughness. Although the manufacturing process for the BOLT model was carefully controlled to maintain a surface roughness below $0.4\,\mu\text{m}$, it remains possible that this level of smoothness was not sufficient to prevent stationary crossflow instabilities, especially considering the very small boundary-layer thicknesses near the leading edges (below $0.5\,\text{mm}$). Stationary crossflow vortices could then serve as a support for secondary instabilities (such as type-I instability).

7. Linear Stability Analysis

7.1. Second Mack and Crossflow Modes at PCB11 location

As a first step, Figure 13 (*left*) presents a comparison between experimental measurements and two distinct instability modes computed from LST: a planar second Mack mode ($\beta = 0 \, \text{m}^{-1}$) and a traveling crossflow mode ($\beta = -750 \, \text{m}^{-1}$). The analysis focuses on Reynolds numbers ranging from 3.24 to $5.06 \times 10^6 \, \text{m}^{-1}$ in the experiments, where a clear spectral bump is observed in the PSDs.

Regarding the second mode, the frequency corresponding to the maximum amplification predicted by LST ($f \approx 142\,\text{kHz}$) aligns remarkably well with the peak observed in the experimental spectra. This agreement supports the conclusion that the second Mack mode is indeed captured by the measure-

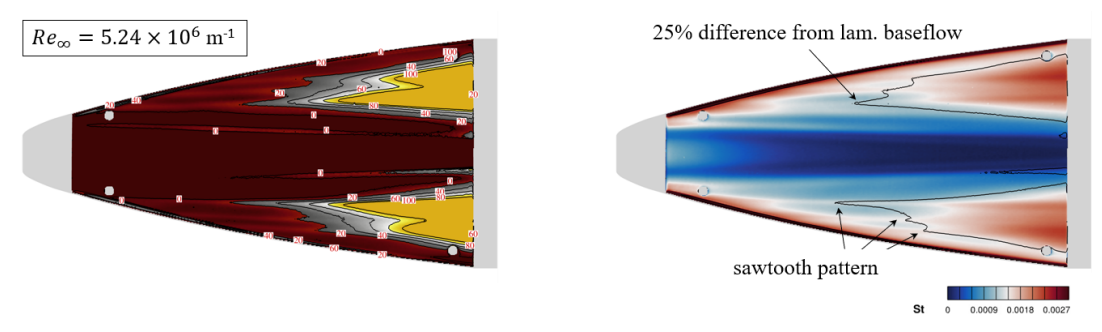


Fig 12. Percentage difference between experiment and laminar simulation (from 0, dark red, to 100%, yellow) (*left*). Experimental wall heat-flux with the line of 25% difference from laminar simulation highlighted (*right*).

ments. In the case of the crossflow mode, the experimental identification is more challenging due to the smaller spectral bump and the limitations of PCB sensors (cutoff frequency at 11 kHz). Nevertheless, the LST predicts a crossflow mode with amplification levels comparable to the second mode, and the corresponding spectral bump observed experimentally falls within the same frequency range. This suggests that traveling crossflow waves have been measured experimentally.

The mapping of the spatial growth rates of the instability modes as a function of the azimuthal angle ψ is shown in Figure 13 (right). For the second Mack mode, the analysis reveals that the most amplified disturbances are slightly oblique, with a maximum amplification occurring around $\psi \approx -20^\circ$ and at a frequency of approximately 132 kHz. Although the amplification rate remains comparable to that of the planar case ($\beta = 0$), this result indicates that the dominant structure is not strictly two-dimensional. This observation is consistent with previous DNS studies conducted by [30] at a higher Reynolds number ($Re \approx 9.9 \times 10^6 \, \mathrm{m}^{-1}$), which also revealed an oblique second-mode lobe on the BOLT configuration. Concerning the traveling crossflow mode, the most amplified disturbances are found at $\psi \approx -80^\circ$, corresponding to a strongly swept orientation with respect to the local flow direction. The associated frequency is around 12 kHz, falling within the range of the low-frequency bumps observed experimentally in the PSDs.

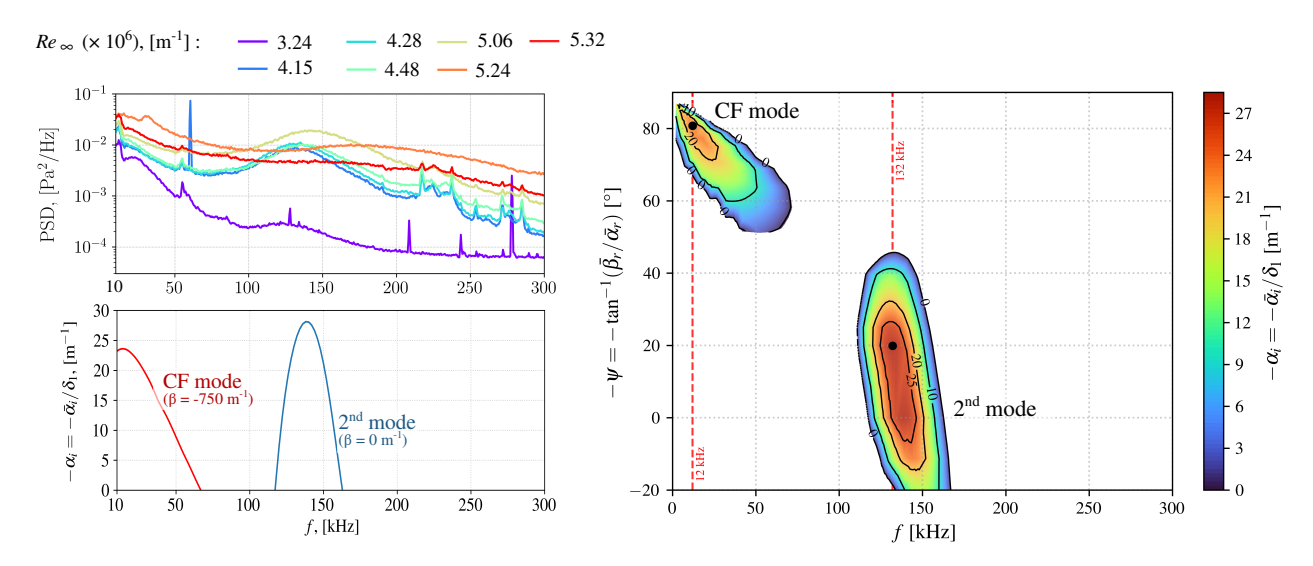


Fig 13. Comparison of experimental PSD with traveling crossflow and second Mack modes from LST (*left*). Evolution of the two modes with the azimuthal angle $\psi = \tan^{-1}(\beta/\alpha_r)$ of the perturbation (*right*).

7.2. N-Factor Calculations

Experimentally, the spatial amplitude growth of the second Mack mode instability is determined using

$$N_{\text{exp}} = \ln\left(\frac{A(f)}{A_0(f)}\right) = \frac{1}{2}\ln\left(\frac{\text{PSD}(f)}{\text{PSD}_0(f)}\right)$$

Here, we consider four sensors (PCB04, PCB06, PCB08, and PCB11) as analysis of their instantaneous signals allows to track wavepackets from PCB04 to PCB11 [18]. Since the initial amplitude of the instability is not known, the reference PSD₀ is taken as the noise floor level of the most upstream sensor [31]. The envelope, shown in Fig. 14, is then determined by taking the highest amplified frequency within the frequency range of the instability. An increase of the maximum amplitude growth is noted for the five cases considered. At $Re_{\infty} = 5.24 \times 10^6 \, \text{m}^{-1}$, the growth reaches $\ln(A_{PCB11}/A_0) = 2.47^{\parallel}$. Such approach could not be applied for the spectral bump associated with crossflow instability as no clear spatial growth was found experimentally.

HiSST-2025-256 Page | 12 L. Sombaert, M. Lugrin, G. Bégou, S. Esquieu, and R. Bur Copyright © 2025 by the authors

Comparisons between experimental results and LST predictions should always be made cautiously as the initial disturbance amplitude in the experiments is unknown.

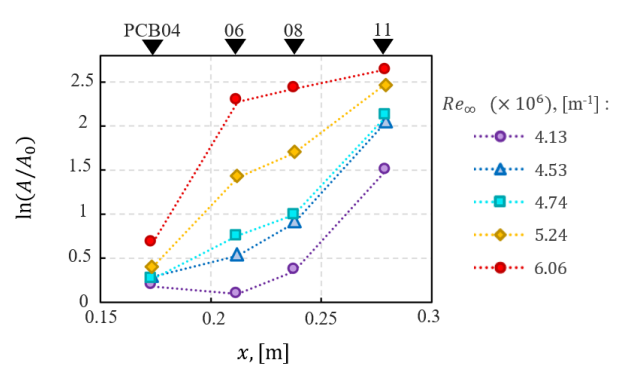


Fig 14. Envelope of the amplitude growth along the outboard ray of PCBs.

The spatial evolution of the planar second Mack mode is presented in Figure 15 (left). The classical instability diagram characteristic of this mode is clearly identifiable. As the flow progresses downstream, the boundary-layer thickens, leading to a reduction in the most amplified frequency. This trend is consistent with the known scaling of the second mode with boundary-layer thickness, which follows approximately $f \approx u_e/(2\delta)$. The onset of the instability appears relatively far downstream (x > 0.23), and the peak amplification is located in the aft region of the body. The corresponding N-factor reaches a maximum value of approximately $N \approx 0.6$, which is considerably below the typical threshold associated with transition onset ($\approx 5/6$). This finding is consistent with previous LST analyses performed on the BOLT configuration at comparable Reynolds numbers [19], which reported similarly low amplification levels. In the same study, the use of more advanced approaches such as the line or plane-marching PSE, yield N-factors of the order of 1.5, closer to the experimental value but still too low to account for transition onset by this mechanism alone.

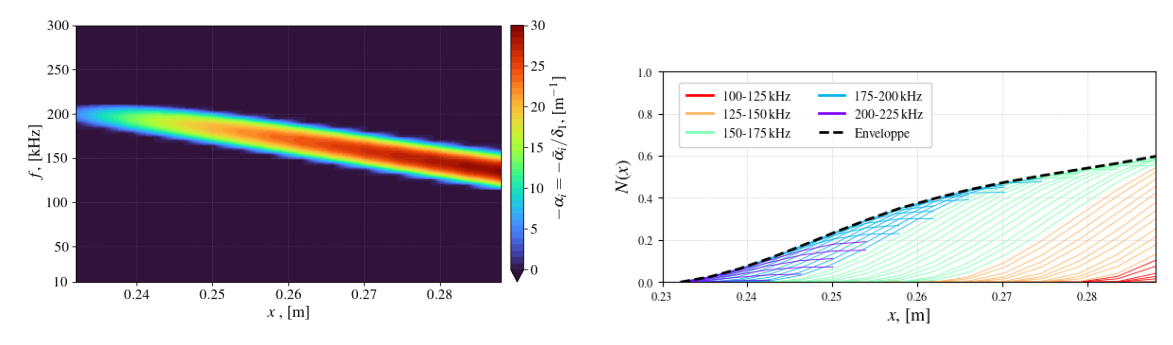


Fig 15. Spatial Evolution of Second Mack Mode (*left*) and computation of the associated *N*-factor (*right*), considering $\beta = 0 \text{ m}^{-1}$, following the meshing line passing by PCB11.

Regarding the evolution of the N-factor associated with the traveling crossflow instability, the maximum amplification reaches approximately $N \approx 1.4$ near the end of the computational domain. This value is again in line with those typically obtained using classical LST applied to BOLT at comparable Reynolds numbers [19]. However, this is significantly lower than the amplification levels predicted by more advanced approaches, which yield N-factors of the order of 4 for crossflow modes, more coherent with transition onset.

Conclusion

This study investigated the nature of flow instabilities over the BOLT geometry in the hypersonic regime (Mach 7), focusing on the outboard region where transition is first observed experimentally. Power spectral density analyses of wall pressure measurements acquired by PCB sensors have revealed two distinct spectral bumps consistently appearing under transitional conditions: one around 20 kHz and another near 150 kHz. Through LST analysis, it was shown that these two frequencies correspond respectively to a traveling crossflow mode (low-frequency, highly oblique structure) and to the second Mack mode (higher-frequency, slightly oblique). However, the analysis of the associated amplification factors (N-

HiSST-2025-256 Page | 13 Copyright © 2025 by the authors

Fig 16. Computation of the *N*-factor of the traveling crossflow mode, considering $\beta = -1250 \,\mathrm{m}^{-1}$, following the meshing line passing by PCB11.

factors) revealed the limitations of applying classical LST to such a complex, three-dimensional flowfield. In both cases (traveling crossflow and second mode), the computed N-factors remained below typical transition thresholds, whereas experimental measurements clearly indicated a transitional regime. This highlights a clear limitation of the local, parallel-flow LST approach for the BOLT configuration. However, the present work demonstrates the utility of combining experimental data with LST as it remains a powerful tool to identify instability modes and, therefore, to help with the physical interpretation of the measurements.

References

- Leyva, I. A. The relentless pursuit of hypersonic flight. Physics today 70, 30-36 (Nov. 2017).
- Sandham, N. & Van den Eynde, J. Outcome of high-speed boundary layer transition workshop at HiSST 2022. CEAS Space Journal 15, 989-991 (Nov. 2023).
- Van Driest, E. R. The Problem of Aerodynamic Heating. Aerodynamic Heating, National Summer Meeting, IAS, Los Angeles (June 1956)
- Lin, T. C. Influence of Laminar Boundary-Layer Transition on Entry Vehicle Designs. Journal of Spacecraft and Rockets 45, 165-175 (Mar. 2008).
- Schneider, S. P. Developing mechanism-based methods for estimating hypersonic boundary-layer transition in flight: The role of quiet tunnels. Progress in Aerospace Sciences 72, 17-29 (Jan. 2015).
- Stetson, K. F. On predicting hypersonic boundary-layer transition tech. rep. AFWAL-TM-87-160-FIMG (Air Force Wright Aeronautical Laboratories, 1987).
- Dolvin, D. J. Hypersonic International Flight Research and Experimentation (HIFiRE) in 15th AIAA/AAAF International Space Planes and Hypersonic Systems and Technologies Conference (Dayton, Ohio, 2008).
- 8. Kimmel, R. L. et al. in 47th AIAA Fluid Dynamics Conference (American Institute of Aeronautics and Astronautics, June 2017).
- Leyva, I. A. & Cummings, R. M. Introduction to the Special Section on the Boundary Layer Transition (BOLT) Flight Experiment. Journal of Spacecraft and Rockets 58, 4-5 (Jan. 2021).
- Wheaton, B. M., Berridge, D. C., Wolf, T. D., Stevens, R. T. & McGrath, B. E. Boundary Layer Transition (BOLT) Flight 10 Experiment Overview in 2018 Fluid Dynamics Conference (American Institute of Aeronautics and Astronautics, Atlanta, Georgia, June 2018).
- Butler, C., Araya, D., McKiernan, G. & Wheaton, B. M. Supersonic Transition Measurements During the BOLT Flight Experiment Descent Phase in AIAA Aviation 2022 Forum (American Institute of Aeronautics and Astronautics, June 27-July 1, 2022, June 2022).
- Kutty, P., Butler, C., Wheaton, B. M. & Fortier, J. 6DOF Simulation Analysis for the Post-Flight Investigation of the Boundary Layer Transition (BOLT) Experiment in AIAA Aviation 2022 Forum (American Institute of Aeronautics and Astronautics, June 27-July 1, 2022, June 2022).
- Meritt, R. J., Molinaro, N. J., Dufrene, A., MacLean, M. & Bowersox, R. D. A Comparative Analysis of In-Flight and Full-Scale Ground Facility Wall Shear Measurements on the BOLT II Vehicle in AIAA SciTech 2024 Forum (Orlando, FL, Jan. 2024).
- McKiernan, G. et al. Initial Results of the BOLT-1B Flight Experiment in AIAA SciTech 2025 Forum (2025).
- Thome, J., Knutson, A. & Candler, G. V. Boundary layer instabilities on BoLT subscale geometry in AIAA SciTech 2019 Forum 15. (American Institute of Aeronautics and Astronautics, San Diego, California, Jan. 2019).
- Berridge, D. C. et al. Hypersonic Ground Tests With High-Frequency Instrumentation In Support of the Boundary Layer 16. Transition (BOLT) Flight Experiment in AIAA SciTech 2019 Forum (American Institute of Aeronautics and Astronautics, San Diego, California, Jan. 2019).
- Thiele, T., Willems, S. & Gülhan, A. DLR AS-HYP Transition Experiments on BOLT-Model in H2K tech. rep. AFRL-AFOSR-UK-TR-2021-0011 (Deutsches Zentrum für Luft- und Raumfahrt, June 2021).
- Sombaert, L. et al. Hypersonic boundary-layer transition on the BOLT forebody in the R2Ch facility. en. Experiments in fluids 18. 66 (June 2025).
- Sombaert, L. et al. Ground Tests on BOLT at Mach 7: Cross-Facility Comparison and Stability Analysis. AIAA journal (2025).
- DAAA/ONERA. Blowdown R1Ch and R2Ch Wind Tunnels: Informative Poster. Accessible via: https://www.onera.fr/sites/ 20. default/files/Departements-scientifiques/DAAA/poster-SR-en.pdf.
- Masutti, D., Spinosa, E., Chazot, O. & Carbonaro, M. Disturbance Level Characterization of a Hypersonic Blowdown Facility. 21 AIAA Journal 50, 2720-2730 (Dec. 2012).

HiSST-2025-256 Page | 14 Copyright © 2025 by the authors

- Threadgill, J. A. et al. Scaling and Transition Effects on Hollow-Cylinder/Flare SBLIs in Wind Tunnel Environments in AIAA 22. SciTech 2024 Forum (American Institute of Aeronautics and Astronautics, Orlando, FL, Jan. 2024).
- 23. Le Sant, Y., Marchand, M., Millan, P. & Fontaine, J. An overview of infrared thermography techniques used in large wind tunnels. Aerospace Science and Technology 6, 355-366 (Sept. 2002).
- Le Sant, Y. An image registration method for infrared measurements. Quantitative infrared thermography journal 2, 207–222 24. (Dec. 2005).
- 25. Berridge, D. C., Wheaton, B. M., McKiernan, G. R., Wolf, T. D. & Arraya, D. FA9550-17-2-0001 Ground Testing Final Report tech. rep. (AFOSR, 2021).
- Liou, M.-S. A sequel to AUSM, Part II: AUSM+-up for all speeds. en. Journal of computational physics 214, 137-170 (May 26. 2006).
- 27. Van Ingen, J. The eN method for transition prediction. Historical review of work at TU delft in 38th Fluid Dynamics Conference and Exhibit (American Institute of Aeronautics and Astronautics, Reston, Virigina, June 2008).
- Bégou, G., Maugars, B., Andrieu, B. & Deniau, H. Boundary-Layer Quantities Extraction from CFD Computations on Complex Geometries: Methods and Application to Vehicle Design in Proceedings of the 3rd International Conference on Flight Vehicles, Aerothermodynamics and Re-entry (FAR) 18-22 May 2025 (Arcachon, France, May 2025).
- 29. Esquieu, S., Benitez, E., Schneider, S. P. & Brazier, J.-P. Flow and stability analysis of a hypersonic boundary layer over an axisymmetric cone cylinder flare configuration in AIAA Scitech 2019 Forum (American Institute of Aeronautics and Astronautics, Reston, Virginia, Jan. 2019).
- Knutson, A. L., Thome, J. S. & Candler, G. V. Numerical Simulation of Instabilities in the Boundary-Layer Transition Experiment Flowfield. Journal of Spacecraft and Rockets 58, 90-99 (Jan. 2021).
- Edelman, J. B. & Schneider, S. P. Secondary Instabilities of Hypersonic Stationary Crossflow Waves. AIAA Journal 56, 182-192 (Jan. 2018).

HiSST-2025-256 Page | 15